Mineralium Deposita (2001) 36: 32–44

ARTICLE

Stephanos P. Kilias · Jon Naden · Ioannis Cheliotis
Thomas J. Shepherd · Heleni Constandinidou
John Crossing · Ioannis Simos

Epithermal gold mineralisation in the active Aegean Volcanic Arc: the Profitis Ilias deposit, Milos Island, Greece

Received: 24 February 2000 / Accepted: 15 July 2000

Abstract The Profitis Ilias gold deposit, located on the western part of Milos Island, Greece, is the first epithermal gold deposit discovered in the Pliocene–Pleistocene Aegean volcanic arc. Estimated ore reserves are 5 million tonnes grading 4.4 g/tonne Au and 43 g/tonne Ag. The deposit is closely associated with a horst and graben structure, and occurs in a series of steep interconnected crustiform-banded quartz veins up to 3 m wide, extending to depths of at least 300 m. The mineralisation occurs in three stages and is hosted by 3.5–2.5 Ma old silicified and sericitised rhyolitic lapilli-tuffs and ignimbrites. It consists of pyrite, galena, chalcopyrite, electrum and native gold. Additionally, adularia occurs with quartz mainly in veins. Homogenisation temperatures of primary liquid-rich inclusions vary from 145 to 399 °C for the ore stage, and 112 to 263 °C for the post-ore stage. Salinities range between 0.1 and 11.4 wt% NaCl equiv. and 0.93 to 8.5 wt% NaCl equiv. for the ore stage and the post-ore stage, respectively. Rare vapour-rich inclusions in ore stage quartz homogenise between 368 and 399 °C and estimates of eutectic melting (−25 to −38 °C) indicate the presence of Ca and Mg in the ore fluids. Sample elevation versus fluid inclusion T_h–salinity relationships show (1) a high-salinity trend, where moderate-temperature (300–250 °C) and moderate-salinity brines (~3 wt% NaCl equiv.) trend to high-salinity (up to 15 wt% NaCl equiv.) fluids with lower (~25–50 °C) homogenisation temperatures, and (2) a high-T_h trend where moderate-salinity and moderate-temperature brines (200–250 °C; 3 wt% NaCl equiv.) develop into low-salinity (< 1 wt% NaCl equiv.), high-temperature (> 350 °C) fluids. These trends are best explained by extreme boiling and vapourisation phenomena between 200 and 250 °C. The 430–450 m asl (metres above sea level) level marks the transition between a lower liquid-dominated segment of the system where only the steep high-salinity trend is seen, and an upper vapour-dominated segment where the high-T_h trend or a combination of both are seen. There is a close spatial association between mineable gold grades and the upper segment of the system. Depth-to-boiling curves suggest that the paleo-surface was ~200 m above the present summit of Profitis Ilias. Comparison of the mineralisation and fluid geochemistry at Profitis Ilias with that of the nearby modern geothermal system indicates that the processes of metal mineralisation have probably been continuous since the Late Pliocene.

Editorial handling: P. Lattanzi

S. P. Kilias (✉)
National University of Athens, Department of Geology,
Section of Economic Geology and Geochemistry,
Panepistimiopolis, Ano Ilisia, 157 84 Athens, Greece
e-mail: kilias@geol.uoa.gr

J. Naden · T. J. Shepherd
British Geological Survey,
Keyworth, Notts NG12 5GG, UK

I. Cheliotis · H. Constandinidou
Institute of Geology and Mineral Exploration,
70 Mesoghion St., 11527 Athens, Greece

J. Crossing
RGC Exploration, P.O. Box 322,
Victoria Park, WA 6100, Australia

I. Simos[1]
Midas S. A., Adamas, GR 84801, Milos, Greece

Present address:
[1] Silver & Baryte Ores Mining Co,
Amerikis 21A,
106 72 Athens, Greece

Introduction

The purpose of this work is to present the first published geological, mineralogical and fluid inclusion data of a productive gold-bearing epithermal system in the Pliocene–Quaternary south Aegean active volcanic arc (SAAVA). We have attempted to decipher the mechanisms of gold deposition and to address the fluid source(s) by comparing the ancient geothermal system with a nearby modern equivalent.

The Aegean region is characterised by active crustal deformation, subduction, high volcanic activity and high heat flow (Fytikas et al. 1984; Jackson and McKenzie 1988; Papazachos and Kiratzi 1996). Volcanic activity, associated with orogenesis, has been nearly continuous since the Oligocene, and is represented by two main belts clearly separated in space and time (Fytikas et al. 1976, 1984):

1. The Oligocene–Miocene north Aegean volcanic belt consists of Lower Oligocene–Middle Miocene calc-alkaline, high-K and shoshonitic volcanics. These have been related to Tertiary subduction of the Aegean microplate (?) under the Rhodope Massif. This volcanic activity progressively migrated southwards and ceased in Middle Miocene (Fytikas et al. 1984).
2. The SAAVA is characterised by Pliocene–Pleistocene island arc calc-alkaline volcanic rocks ranging from basalts to rhyolites, with predominantly andesites and dacites. The arc results from north-eastward subduction of Mediterranean sea floor (part of the African plate) below the Aegean microplate (McKenzie 1970; Papazachos and Comninakis 1971; Le Pichon and Angelier 1979. Dewey and Sengor 1979). Moreover, it may be considered to be an active analogue of the subduction-related magmatic arcs that were operating in the Carpatho–Balkan region during Late Cretaceous to Pliocene. To date, information concerning mineralisation in the SAAVA is restricted to confidential and unpublished data (Alfieris 1993; Murray and Petrakis 1993; Spartali 1994).

The Profitis Ilias gold deposit, located on Milos Island is located 10 km WSW from an active geothermal system (Fig. 1). The modern geothermal system is two-phase and high-enthalpy (> 1700 kJ/kg; 310–320 °C), and the reservoir is located ~1200 m below the present-day surface. This close spatial relationship with an active geothermal system makes Profitis Ilias unique among epithermal deposits in the Carpatho-Balkan and Aegean regions.

Geology and mineralisation of Milos Island

The geology, geochronology, geothermal activity and structure of Milos Island are described in detail by Fytikas (1977), Fytikas et al. (1976, 1984, 1986, 1989), Briqueu et al. (1986), Fytikas (1989), Papanikolaou et al. (1990), Liakopoulos et al. (1991) and Tsokas (1996), and only a summary is given here. The rocks, which make up the island, can be divided into four main lithological units (Fig. 1).

1. The oldest rocks on the island consist of Alpine metasedimentary rocks. They include micaschists,

Fig. 1 Geological map of Milos Island, showing the location of Profitis Ilias and the Mn–Ba, Pb–Zn–Ag mineralisations at Cape Vani, and Triades-Galana (modified after Fytikas 1977)

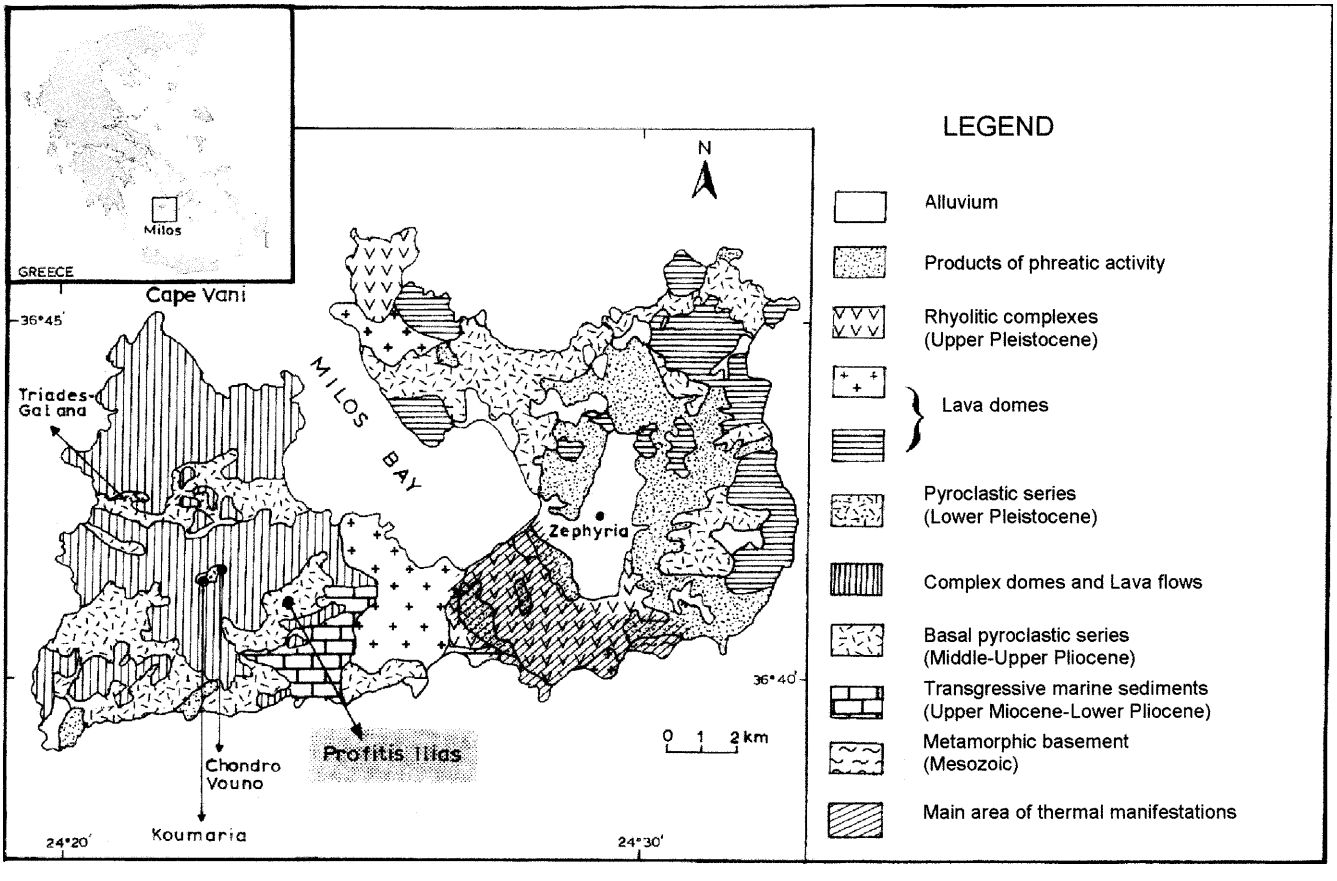

calcareous schists with intercalated lavas and calcareous rocks, chloritic schists, and quartzites, which were metamorphosed to blueschist (64.2 ± 6.5 Ma) and greenschist facies (35.2 ± 1.0 Ma).
2. Unconformably overlying the metamorphic basement is a sequence of Upper Miocene–Lower Pliocene transgressive marine sediments consisting mainly of limestones, marls and conglomerates. These rocks form the platform sediments on which the volcanic island is built. It is important to note that there are no known evaporite sequences within the marine sediments.
3. Volcanism, on the western part of Milos, commenced 3.5 Ma. The oldest volcanic rocks comprise felsic pumice flows, tuffs, ignimbrites and tuffites, which make up the Basal Pyroclastic Series (3.5–2.5 Ma). This lower sequence is overlain by dome complexes and lava flows (2.5–2.0 Ma), which are accompanied by andesitic to dacitic pyroclastic material.
4. The eastern and central parts of the island are made up of a younger volcanic suite (the Pyroclastic Series), consisting of rhyolitic complexes (1.9–0.1 Ma) comprising lahars and tuffs accompanied by rhyolitic to rhyodacitic domes and flows.

In the west, the structure of Milos is dominated by NEE–SWW and E–W trending faults, whilst in the east the most significant fault trend is N–S. The central part of the island (Milos Bay) is controlled by NW–SE trending faults, and constitutes a graben structure, bounded by horsts to the east and west. Metalliferous mineralisation occurs mainly in western Milos, where it is controlled by E–W trending horst structures. At Profitis Ilias, the older Basal Pyroclastic Series hosts the gold mineralisation (Fig. 1).

Although the last recorded volcanism was ~100,000 years ago, Milos is still an active geothermal field. Present-day activity is concentrated in the central and eastern portions of the island, expressed by fumaroles, hot springs, hot ground, and submarine gas escapes, which occur in the E–SE part of the island (Fig. 1). In 1982–1983, the Public Power Corporation of Greece operated an experimental geothermal power plant in the eastern part of the island (Zephyria; Fig. 1).

Milos Island hosts a significant number of actively exploited industrial mineral deposits, which were formed in an environment of high heat-flow and geothermal activity (Hauck 1983; Ericsson et al. 1992; Christidis et al. 1995; Christidis and Scott 1997). In addition to industrial minerals, Milos also produced silver and lead at Triades-Galana, and manganese at Cape Vani (Fig. 1). At Cape Vani, mineralisation occurs in stratiform and vein types (Liatsikas 1955; Liakopoulos 1987). The stratiform mineralisation comprises mainly primary, and secondary Mn-oxides. Vein-type mineralisation consists of quartz, barite, Mn-calcite, quartz, various sulphides and barite (Liakopoulos 1987). Its genesis is the result of diagenetic replacement and submarine precipitation from brines mixed with seawater (Liakopoulos 1987; Galanopoulos and Koinakis 1991). Mineralisation at Triades-Galana comprises Pb–Zn–Ag sulphide and Ag-bearing barite ores. They are structurally controlled and associated with zones of silicification and argillisation. Mineralisation occurs as (1) interstitial material to silicified and hydrothermally brecciated tuffs, (2) sulphide fracture-fillings, and (3) argentiferous barite veins and impregnations (Voreadis and Mourabas 1935). Field evidence suggests these ores are epithermal in origin.

The Profitis Ilias deposit is one of several gold-bearing epithermal quartz veins in the area, which include the Koumaria and Chondro Vouno (Amethyst) prospects to the N and NW (Fig. 1). The first discovery of gold in this area was in 1987 by Ian Plimer and John Nethery in a joint venture with Niugini Mining (J. Nethery, personal communication). In 1993 Kostas Salonikos (Silver and Barite Co.) first sampled the main Profitis Ilias veins and a year later a joint venture drilling programme was commenced by Silver and Barite, Niugini Mining and Renison Gold Corporation (Midas S.A.). Estimated reserves at Profitis Ilias are 5 million tonnes of ore, grading at 4.4 g/tonne gold and 43 ppm silver. Recently, RoyalGold Inc. discovered new gold reserves at the Chondro Vouno prospect. These amount to 2.2 Mt grading 5.14 g/tonne Au (cut-off grade 2.5 g/tonne) or 3.3 Mt grading 4.2 g/tonne (cut-off grade 2 g/tonne) (RoyalGold news release; www.royalgold.com/news/990615.htm).

Materials and methods

Sampling

A total of 127 samples were collected from surface exposures (27 samples) and drill core (100 samples) for mineralogical, mineral chemistry, and fluid inclusion studies.

Electron microprobe and X-ray diffraction analyses

Electron microprobe analysis of gold was undertaken using a JEOL superprobe 733 electron microprobe analyser with a Tracor Energy Dispersive Spectrometer operated at 20 kV with a 3-nA beam current and 20-s counting time. Mineral standards were used and ZAF corrections were carried out on-line. X-ray diffraction analyses of alteration and oxidation minerals were performed using an automatic Siemens D500 X-ray diffractometer. Qualitative determination was done with SIEMENS software Diffrac AT 3 using the JCPDS database.

Microthermometry

Fluid inclusion data were obtained on drill-core and surface samples. In total, 23 samples were selected for fluid inclusion microthermometry. These included typical examples of the pre-ore, ore and post-ore mineralisation. For fluid inclusion microthermometry, samples were prepared as free-standing, 100- to 200-μm-thick doubly polished wafers. Analyses were carried out using a Linkam TMSG600 heating–freezing stage calibrated with natural carbon-dioxide-bearing fluid inclusions of known composition and commercially available chemical standards. Estimated analytical error is ±0.2 °C for low (< 50 °C) and ±2 °C for higher (> 75 °C)

temperatures. Elevation data and metal concentrations (Au, Ag, Pb and Zn) were provided by Midas S.A. (Table 1).

Bulk analysis of fluid inclusion volatiles

A selected number of samples (nine) (Table 1) were prepared and analysed for bulk volatiles (H_2O and CO_2). Crushed vein quartz was sieved, washed and ultrasonically cleaned. The samples were then sequentially cleaned in hot (90 °C) HCl and de-ionised water. They were then handpicked, producing a quartz concentrate (~500 mg) free of mineral impurities, and ultrasonically cleaned using dimethylchloride. Inclusion volatiles were released by decrepitation under high-vacuum and analysed manometrically and by quadropole mass-spectrometry (Shepherd et al. 1991).

The main objective of this exercise was to provide estimates of the carbon dioxide content of the fluid inclusions. This data can then be used to correct salinity estimates made from last ice-melting temperatures (Hedenquist and Henley 1985). In addition, it also provides an important parameter for calculating depth to boiling relationships in epithermal systems (Bodnar et al. 1985; Hedenquist and Henley 1985).

Results

The Profitis Ilias deposit

Host rocks to the Profitis Ilias mineralisation are rhyolitic lapilli tuffs and ignimbrites. Field observations suggest the host pyroclastics are in structural contact with a flow banded rhyolite cryptodome (Fig. 2). Mineralisation (electrum, native gold, minor sphalerite, galena, chalcopyrite and pyrite) is developed in a series of veins closely associated with a horst and graben structure. The deposit comprises a series of interconnected steeply dipping (45–80°) to vertical N–S- to NE–SW-trending quartz veins and vein sets. These occupy an arcuate fault network in the western part of the Profitis Ilias horst (Fig. 2). Vein widths are up to 3 m across and extend to depths of at least 300 m below the present-day surface.

The veins are contained within a fault-bounded horst block and although there is post-mineralisation faulting (Fig. 2), this is mainly confined to its margins. The central portions of the block, where most of the samples were taken, have remained stable and the vein sets are still in their original relative positions. Thus, direct comparison between samples collected from different elevations are valid, as the present-day relative positions and those during mineralisation are similar. In addition, the observed regularities in data distribution (see Figs. 7 and 8) witness against any substantial post-mineralisation tectonic disturbance of the vein system.

A systematic investigation of alteration patterns is outside the scope of the present study. However, alter-

Table 1 Summary of fluid inclusion data with corresponding assay and depth information

Surface/ drill hole no.	Sample no.	Elevation (m asl)	Elevation and geochemical data				Salinity (wt% NaCl equiv.)				Th (°C)			Gas data mol% CO_2
			Au (ppm)	Ag (ppm)	Host mineral	*n*	Med.	Min.	Max.	*n*	Med.	Min.	Max.	
Surface	MI-9[a]	645	–	–	Quartz	2	4.1	2.0	6.1	2	291	246	335	0.62
	MI-4	645	–	–	Barite	5	4.7	4.2	5.8	19	192	112	330	
	MI-21[a]	645	–	–	Quartz	9	5.9	2.5	10.2	10	245	145	368	
PD5	2151	642	6.3	197	Barite	6	7.3	3.0	8.5	6	153	150	178	
					Quartz	7	3.4	3.3	5.5	10	276	178	355	
PD10	G2374A	552	2.3	10	Quartz	7	8.2	5.5	9.2	7	207	202	230	
	G2424	421	6.3	17	Quartz	26	6.8	0.0	13.7	26	237	215	253	0.25
	G2416	429	4.2	50	Quartz	19	11.3	4.7	15.5	21	229	206	311	0.43
	G2395	507	3.5	9	Quartz	20	6.9	2.5	12.2	21	220	205	235	0.21
	G2374	552	2.3	10	Quartz	7	4.4	3.4	5.6	7	210	190	234	0.70
PD9	G2283	365	3.6	88	Quartz	6	4.1	3.1	6.2	8	240	219	251	
	G2268	403	10.2	11	Quartz	7	7.4	4.4	9.2	8	212	208	231	0.30
	G2267[a]	405	8.5	3	Quartz	4	7.1	6.5	7.8	6	232	223	249	
	G2255[a]	457	4.8	15	Quartz	11	3.8	3.1	4.7	11	209	190	219	
	G2245[a]	499	18.0	13	Quartz	3	4.2	3.3	4.9	3	213	205	215	
	G2235[a]	529	1.2	11	Quartz	11	3.4	0.5	5.6	11	300	230	389	0.50
PD8	G2185	657	7.2	20	Barite	2	6.5	6.1	6.8	2	155	150	160	
					Quartz	12	6.4	1.5	8.2	12	212	150	399	
PD4	G1873[a]	516	12.9	17	Quartz	3	5.5	4.9	7.0	6	228	187	273	
	G1871	520	1.6	13	Quartz	12	5.0	0.8	6.7	14	216	190	398	
	G1833	578	3.8	5	Quartz	29	8.0	1.0	15.0	29	220	170	400	
	G1810[a]	612	15.1	265	Quartz	1	4.5	4.5	4.5	2	223	161	284	0.43
PD2	G1746[a]	621	56.5	62	Quartz	8	5.3	5.0	5.5	8	230	213	243	0.45
	G1745[a]	622	17.1	31	Quartz	2	2.8	1.7	3.9	3	213	205	232	
PD12	398-5	208	0.1	<2	Quartz	11	5.9	4.1	12.3	11	249	233	269	
	321-6	270	1.1	31	Quartz	28	8.1	4.4	13.7	30	260	237	289	
					Sphal.	–	–	–	–	2	290	285	295	
	380-0	380	–	–	Quartz	15	9.2	6.5	13.9	15	250	237	280	
	325-0	325	7.9	–	Quartz	6	9	7	11	6	257	230	292	
					Total	279	6.7	0.0	15.5	316	112	400	231	

[a] Samples where native gold was observed in the fluid inclusion water

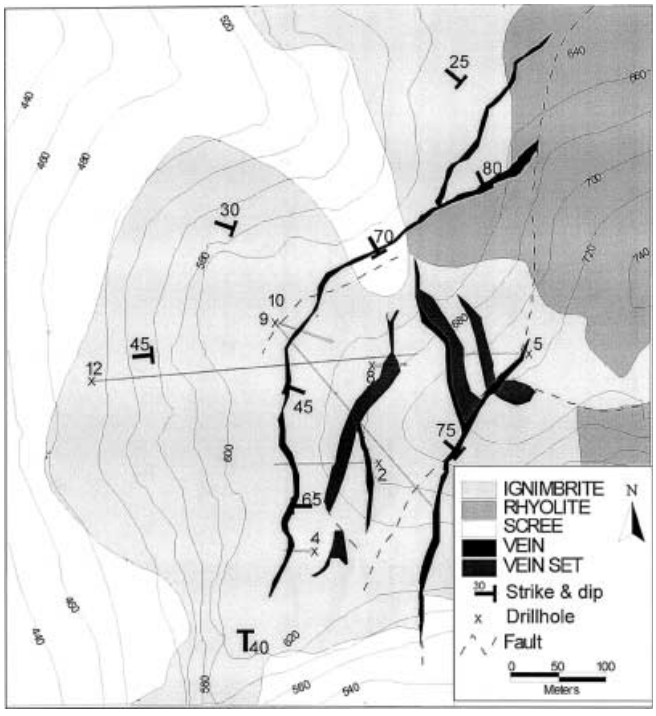

Fig. 2 Geological sketch map of the Profitis Ilias deposit

ation minerals were identified in drill core and surface samples adjacent to the veins. Silica occurs as mosaic-textured microcrystalline quartz, cryptocrystalline chalcedonic quartz, and rarely opal. Adularia is seen with quartz in open space fillings, veins and veinlets (Fig. 3A), as colloform-banded aggregates with chalcedonic quartz, or as fine-grained mosaic-textured aggregates with microcrystalline quartz. Adularia also occurs disseminated in the host rocks adjacent to the veins. Clay minerals (kaolinite, illite, with lesser montmorillonite) occur as fine-grained clusters and matted aggregates within a siliceous matrix. Sericite was seen as fine-grained aggregates and rare veinlets in microcrystalline quartz. In addition, coarser muscovite and accessory pyrite also occur with sericite. Rare alunite and chlorite occur with the clay minerals. Alunite was only found in surface samples and is probably supergene in origin. Pyrite forms micron-sized equant crystals disseminated

Fig. 3 **A** Veinlet of sub-rhombic adularia crystals in hydrothermally altered wallrock, adjacent to vein margin – ore-stage (transmitted light, crossed polars). **B** Development of variable grain-size quartz; note coarse-grained quartz projecting into vugs – ore-stage (transmitted light, crossed polars). **C** Hand specimen of typical 'banded' quartz. **D** Photomicrograph under crossed polars of a cross section through a euhedral coarse-grained quartz crystal showing growth zones defined by dark bands of primary fluid inclusions. Also shown is an example of a two-phase fluid inclusion within a clear part of the quartz crystal (ore stage)

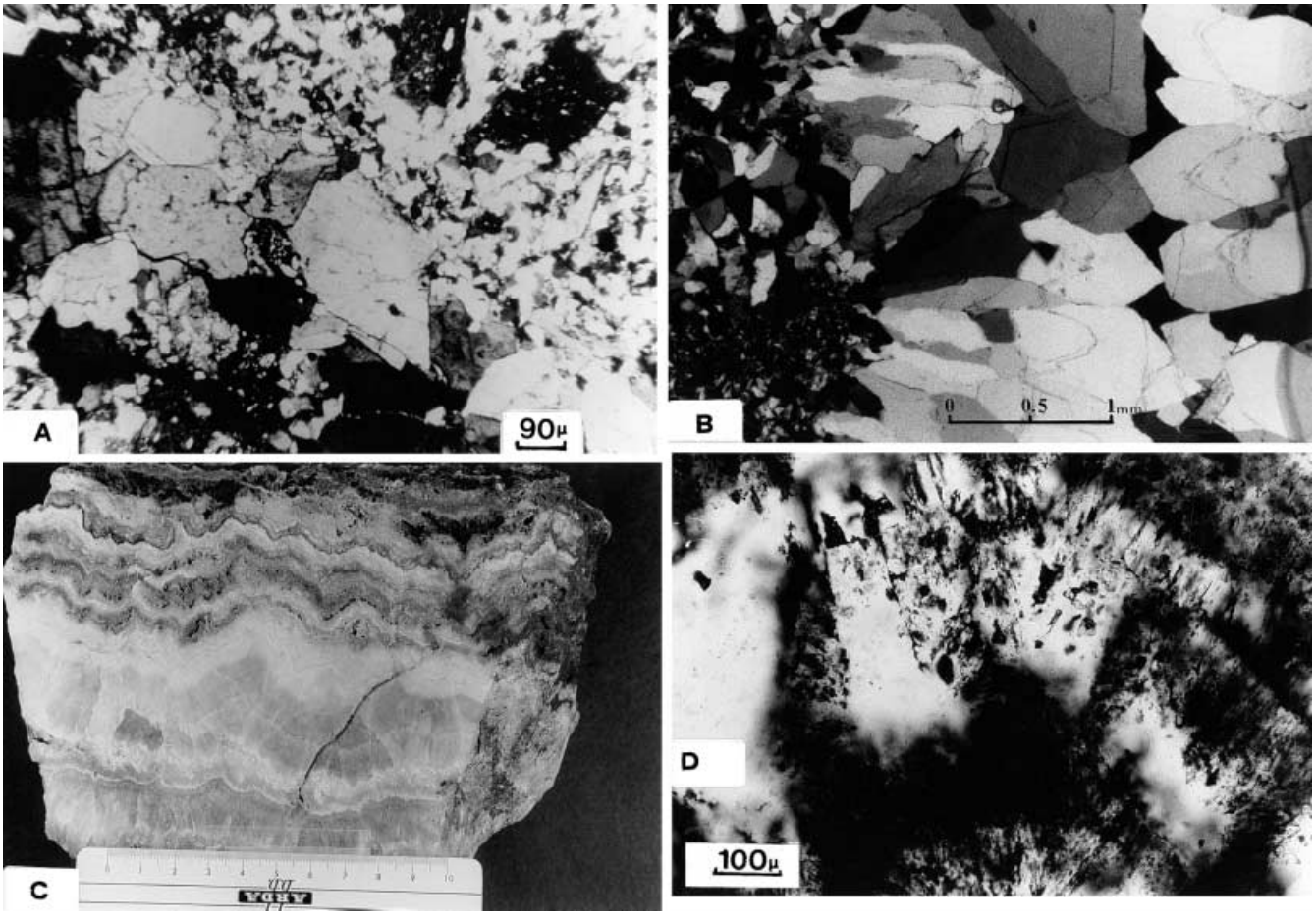

through the silicic matrix, and larger grains and aggregates up to ~0.6 mm in size.

Mineralogy – mineral chemistry and paragenesis

Through microstructural evidence, paragenetic relationships of the vein mineralisation can be represented by a sequence consisting of hypogene pre-ore, ore, post-ore and supergene oxidation stages (Fig. 4).

The earliest phase of mineralisation, which predates gold mineralisation, consists of barren microcrystalline quartz and pyrite. The main ore stage is characterised by deposition of coarse- and fine-grained quartz (Fig. 3B), adularia, sulphides and precious metals. Gold-bearing quartz veins are commonly composite and crustiform-banded. Crustification growth banding consists of marginal fine-grained quartz to fine-grained chalcedony, with coarse-grained comb-quartz occupying the central portion of the vein (Fig. 3C). In order of decreasing abundance, the main sulphide phases comprise sphalerite, pyrite, galena, chalcopyrite, bornite, marcasite, tetrahedrite and Sb–Ag–Cu sulphosalts. Post-ore mineralisation comprises barite intergrown with fine-grained quartz and more rarely with galena, sphalerite, pyrite and chalcopyrite. Lastly, the supergene mineralisation consists of native gold, electrum, silver halides, copper sulphides and carbonates, iron oxides, lepidocrocite, tenorite, cerussite, Pb and Zn carbonates, Fe–Al hydroxides, alunite and Mn-oxides.

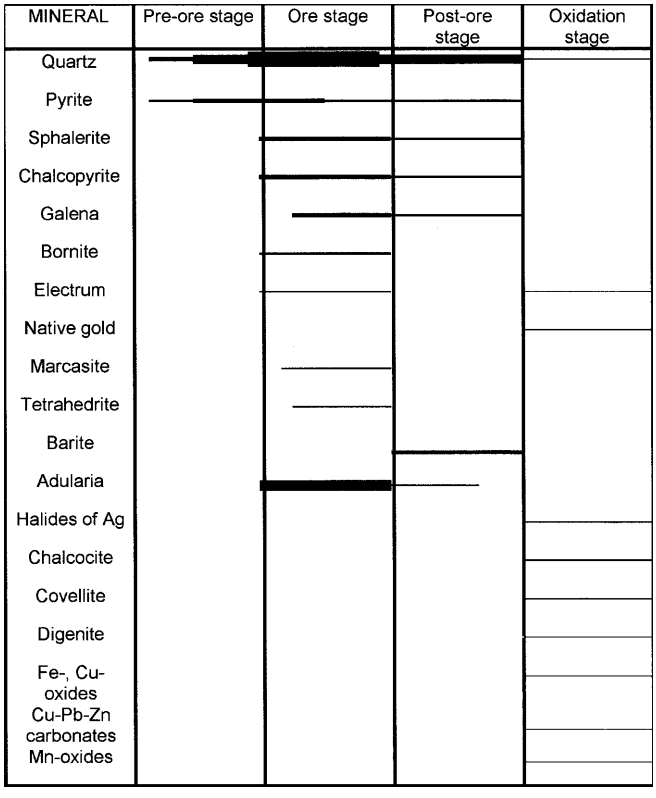

Fig. 4 Generalised paragenetic scheme for the Profitis Ilias mineralisation. *Line width* indicates abundance

Sphalerite occurs as either subhedral coarse grains in ore-stage assemblages or as anhedral to subhedral fine-grained crystals included in post-ore barite. Three characteristic textural forms of pyrite are recognised. The earliest generation occurs as fine-grained cubic crystals disseminated in pre-ore microcrystalline quartz. The second is present as coarser-grained subhedral to anhedral grains associated with other ore-stage minerals. It is characteristically zoned with chalcopyrite blebs defining individual growth zones. The latest pyrite is intergrown with barite in the post-ore assemblages. Galena occurs as coarse-grained patches in the main ore-stage, whilst a later type is included in post-ore barite. In addition, fine-grained galena forming thin rims around early coarse-grained sphalerite was observed. Here it is intergrown with secondary copper sulphides and is believed to be of supergene origin (Ramdohr 1980). Chalcopyrite occurs disseminated in the main ore-stage quartz or along growth zones in pyrite, and as inclusions in barite.

In total, native gold was observed in 16 samples. All of these were located at elevations >430 m asl (Table 1). Gold was not observed in any polished sections collected below this elevation. It is typically very fine grained (0.5–30 μm) and occurs in three distinct chemical and mineralogical associations (Constantinidou et al. 1998).

1. Isolated electrum grains with silver-enriched rims (fineness 610–728). These occupy interstices between, or are included in ore-stage fine-grained quartz (fineness = 1000 × [wt% Au/(wt% Au + wt% Ag)]; Morrison et al. 1991).
2. Electrum grains with silver-depleted rims (fineness 656–1000), which are included in goethite, covellite, or are in contact with clay minerals, in the oxidation stage.
3. Pure native gold grains (fineness ~1000), associated with iron and copper oxides and supergene silver halides (iodyrite and cerargyrite) of the oxidation stage.

Bulk volatile analysis

Carbon dioxide contents, for the nine samples analysed, are generally low. They vary from 0.21 to 0.70 mol% carbon dioxide (Table 1), with a median value of 0.43 mol% CO_2.

Fluid inclusion microthermometry

Two main types of liquid–vapour inclusions were identified. Type I inclusions are liquid-rich (<25% vapour), whereas type II inclusions are vapour-rich (>50% vapour). Both occur in quartz, sphalerite and barite.

However, inclusions, suitable for microthermometry, do not occur in pre-ore quartz. Quartz and sphalerite contain predominantly liquid-rich primary inclusions, and in any one sample, these comprise >99% of the fluid inclusion population. Barite, compared with quartz and sphalerite, contains relatively more vapour-rich inclusions (20%).

Fine-grained quartz contains elongate, rectangular or ovoid (sub-rounded) inclusions, which occur either isolated or in sparse clusters. Coarse-grained quartz contains mainly irregularly (stringy) shaped inclusions (up to 25 μm in length) occurring along or oriented perpendicular to, crystal growth surfaces (Fig. 3D). Barite contains larger elliptical to sub-rounded liquid-rich inclusions, locally co-existing, in a random three-dimensional distribution, with oval-shaped vapour-rich inclusions. Intragranular micro-fractures containing all vapour-rich inclusions (up to 50 μm long) exist exclusively in barite. Sphalerite contains a few liquid-rich inclusions with negative crystal shapes with random distributions (15–20 μm long).

The fluid inclusions selected for microthermometric analysis were primary in origin and did not show any evidence of necking (cf. Roedder 1984).

Accurate first melting temperatures (T_{fm}) were difficult to determine and were only recorded in ~15% of inclusions (Fig. 5A). The T_{fm} data range from −25 to −38 °C (Fig. 5A), indicating that, in some inclusions, there is a divalent (Ca, Mg) component to the brine (Sterner et al. 1988). Final ice melting (T_{ice}) was recorded in 266 inclusions in ore-stage quartz and ranged from −11.5 to 0.0 °C (median: −4.2 °C), corresponding to salinities between 0.0 and 15.5 wt% NaCl equiv. (median: 6.7 wt% NaCl equiv. – salinities estimated using Bodnar 1993). In terms of ore-stage quartz type, inclusion salinity varied from 0.5 to 9.2 wt% NaCl equiv. in fine-grained quartz (median: 5.0 wt% NaCl equiv.; $n = 55$) and from 0.0 to 15.5 wt% NaCl equiv. in coarse-grained quartz (median: 5.8 wt% NaCl equiv.; $n = 211$). The distribution of salinity data indicates that there is little statistical difference between the different quartz types (Fig. 5B).

Ice melting was measured in a limited number of inclusions hosted in post-ore barite. Here, ice melting ranges from −5.5 to −1.8 °C (median: −3.6 °C; $n = 13$). This corresponds to salinity variations between 3.0 and 8.5 wt% NaCl equiv. and is within that shown by ore-stage quartz.

Primary, ore-stage quartz, liquid-rich inclusions exhibiting bubble point homogenisation ($L + V \rightarrow L$), did so at temperatures varying from 145 to 400 °C (median: 232 °C; $n = 287$). In terms of quartz type, inclusions in fine-grained ore-stage quartz homogenised from 190 to 400 °C (median 231 °C; $n = 62$), whilst in the coarse-grained quartz T_h ranged from 145 to 399 °C (median 232 °C; $n = 221$). The distributions of these data are illustrated in Fig. 5C, which shows little statistical difference between the various host quartz types. Dew point homogenisation ($L + V \rightarrow V$) was rare in occurrence and occurred between 368 and 399 °C (median = 395; $n = 4$).

Limited homogenisation data were also obtained for sphalerite and post-ore barite. Bubble point homogenisation in sphalerite occurred from 290 to 295 °C ($n = 2$). More determinations were made in barite and, again, inclusions exhibited bubble point homogenisation, but

Fig. 5 Histograms showing the distribution of **A** first-melting temperatures, **B** salinity and **C** homogenisation temperatures (°C). Data are discriminated according to quartz type. Note the homogenisation temperature histogram includes data for dew point homogenisation (four values at 368, 393, 397 and 398 °C)

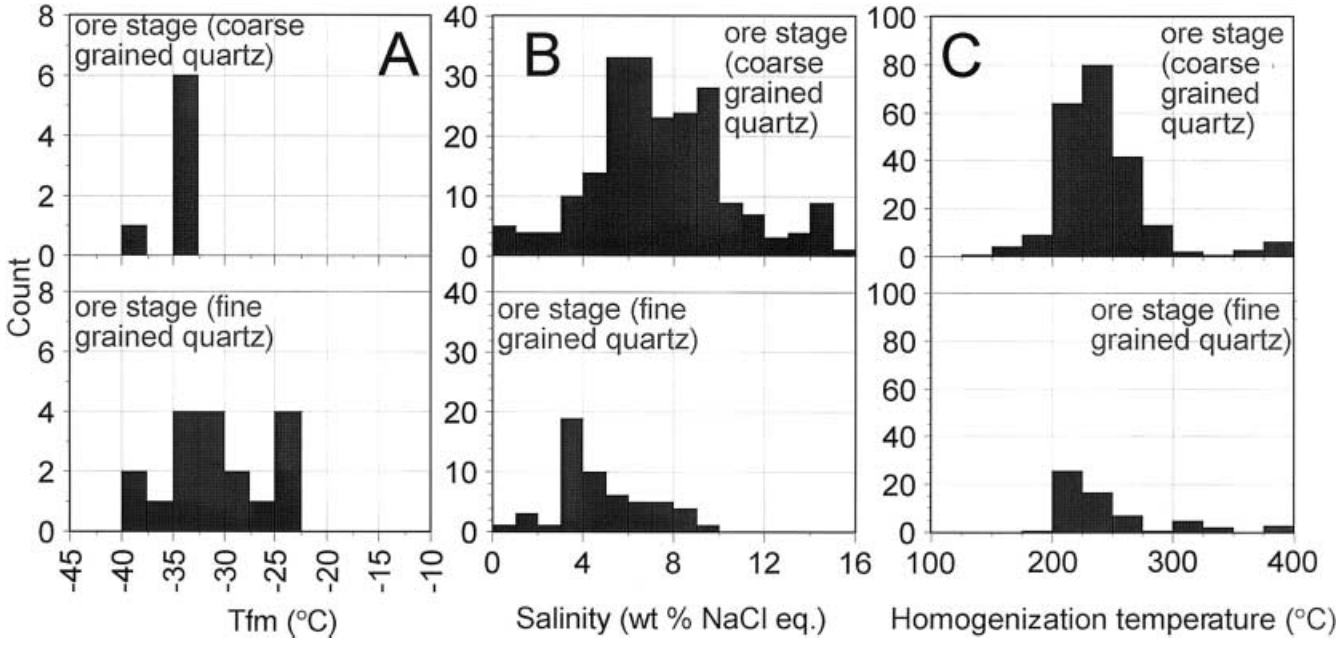

at lower temperatures (112–330 °C, median: 178, $n = 27$). However, fluid inclusions in barite are extremely susceptible to stretching during heating runs and the high homogenisation temperatures in barite must be treated with caution.

Salinity versus temperature trends

Salinity versus temperature data from Profitis Ilias are presented in Fig. 6 with individual points differentiated according to the morphological type of host quartz (fine or coarse grained). The data show that overall inclusion homogenisation temperature and salinity are independent of quartz type. They also show a fair degree of scatter, and individual trends are not easily discernible. However, close examination suggests that most of the data fall within a broad band with moderate variation of homogenisation temperature (200–275 °C) with strongly varying salinity (1–16 wt% NaCl equiv.). In addition to this broad trend, there is a more diffuse trend of decreasing salinity (3–0.5 wt% NaCl equiv.) with increasing homogenisation temperature (225–400 °C). Although careful examination of Fig. 6 reveals two trends, it would be difficult to attribute these to processes such as boiling or mixing. Moreover, it could be argued that the diffuse trend of decreasing salinity with increasing homogenisation temperature results from the necking down of inclusions.

However, by splitting the data on an elevation basis, clear and distinct trends and data distributions become evident.

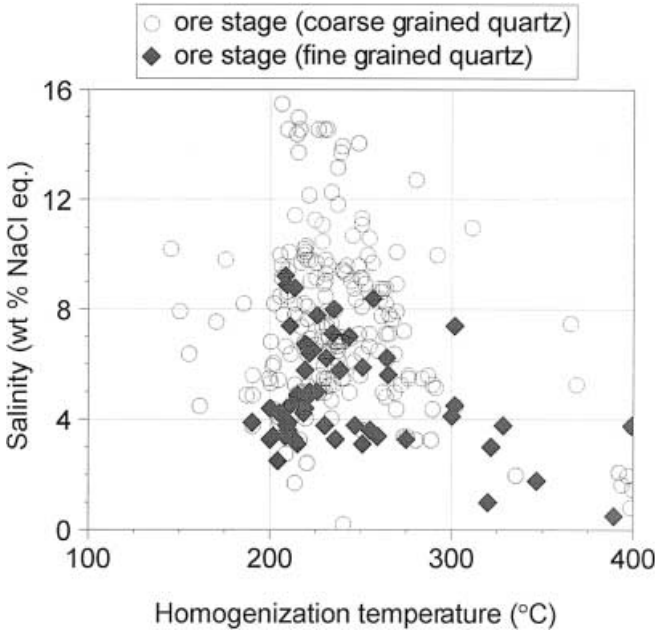

Fig. 6 Homogenisation temperature and wt% NaCl equivalent data for ore-stage quartz hosted fluid inclusions, with data distinguished by quartz type (see text for discussion)

1. A *high-salinity trend*, where vertical to sub-vertical trends of rapidly increasing salinity (3–15 wt% NaCl equiv.) are associated with a gradual decrease (250–200 °C) in homogenisation temperature. This can be seen at elevations of 200–250, 250–300, 350–400, 400–450 and 500–550 m (Fig. 7A, B, D, E, G).
2. A *high-T_h trend*, where a diffuse trend of decreasing salinity with increasing homogenisation temperature is now strongly developed. This type of distribution occurs at elevations of 450–500 and 600–650 m (Fig. 7F, I), and is also present at elevations of 500–550 and 550–600 m (Fig. 7G, H). Previously, it was alluded that this high-T_h trend could be the result of necking down of fluid inclusions. However, the inclusion selection criteria were identical for each sample. Thus, if necking is the cause then the trend should be present at all elevations. This is clearly not the case. It is only present in samples collected >450 m asl. Therefore, the trend must be explained in terms of paleofluid evolution and/or trapping processes.
3. In addition to the above, elevation also exerts a control on trend-type. Below 450 m asl only the steep high-salinity trend is seen. Whereas above this elevation either the high-T_h trend (Fig. 7F, I) or a combination of high-salinity and high-T_h trends are seen (Fig. 7G, H).

T_h versus elevation relationships

Another common method for displaying fluid inclusion data from epithermal environments is to plot homogenisation temperature against elevation. Figure 8 shows how homogenisation temperatures vary with elevation at Profitis Ilias.

In addition to the homogenisation temperature–elevation data, a depth to boiling curve was calculated according to the methodology of Hedenquist and Henley (1985), taking into account the typographical error in Eq. (13), p. 1391. Also, as the fluids at Profitis Ilias are reasonably saline it is necessary to compensate for the effect of dissolved salts on the solubility of CO_2. K_h values for a 5 wt% NaCl solution with a dissolved CO_2 content of 0.5 mol% were obtained from Ellis and Golding (1963). Also, conversion of pressure to depth assumes a hydrostatic gradient. The concentration of CO_2 was estimated from gas analysis data (Table 1) and 5 wt% NaCl corresponds reasonably closely to the median salinity of the Profitis Ilias fluids.

In extinct geothermal systems, to enable 'depth to boiling' curves to be plotted on an elevation-T_h graph, it is necessary to constrain the relative position of the paleo-surface to present-day elevations. This has been undertaken for three scenarios. The first assumes that paleo-surface was at the same elevation as the present-day surface (+0 m curve; Fig. 8). The second infers that the paleo-surface was 100 m above the summit of Profitis Ilias (+100 m curve; Fig. 8). Whilst the third

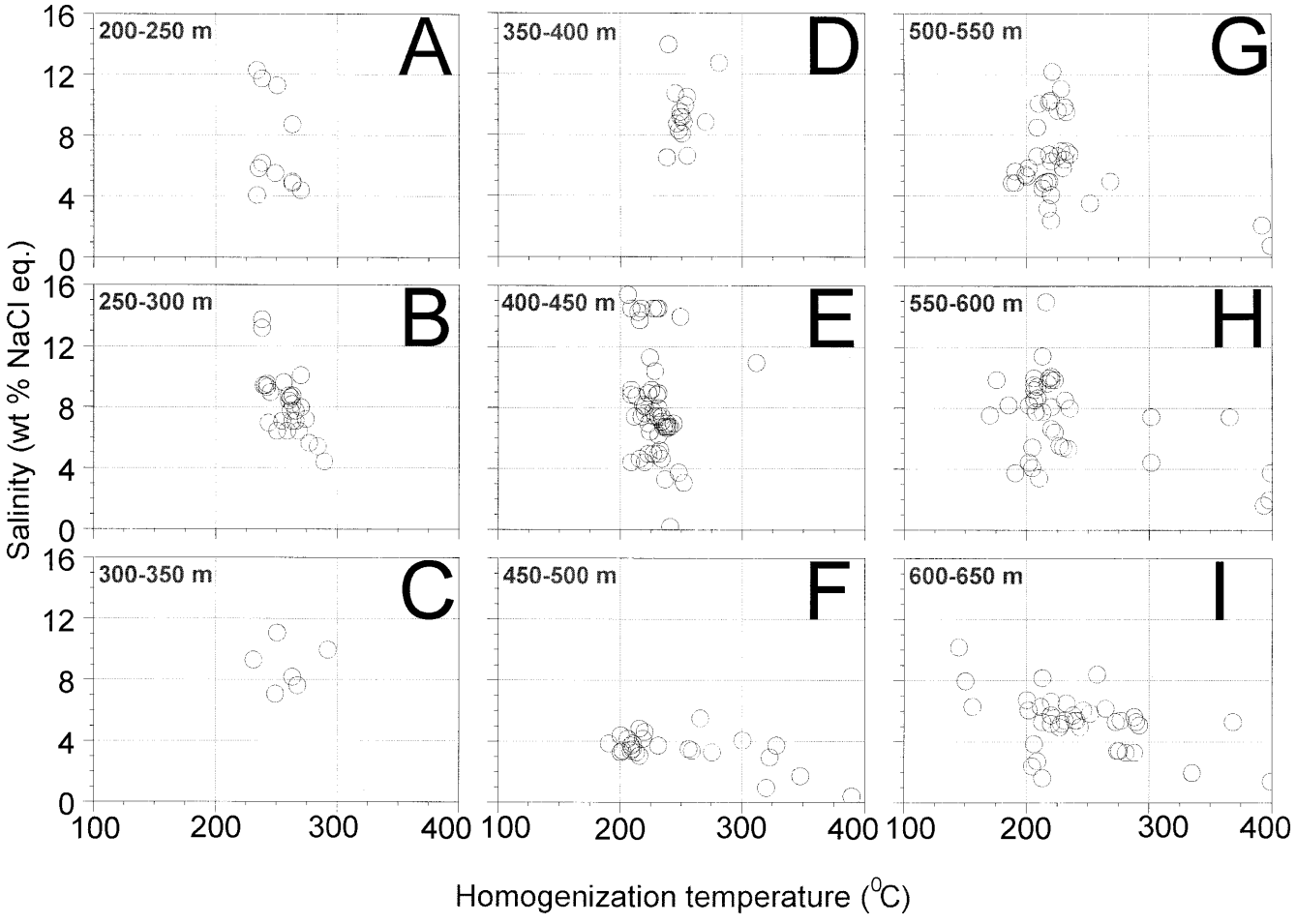

Fig. 7A–I Homogenisation temperature and wt% NaCl equivalent data for ore-stage quartz-hosted fluid inclusions, with data distinguished by sample elevation (see text for discussion)

presumes that net uplift and erosion have resulted in the present-day surface being 200 m below the paleosurface (+200 m curve; Fig. 8). Unlike the histograms presented in Fig. 5C, it is now possible to see two distinct populations of homogenisation temperature. Below 430 m asl only tightly clustered homogenisation temperatures are observed, whilst above this level samples exhibiting a wide range in homogenisation temperature predominate. This distribution shows a correlation with assay data (Fig. 9). Below 400 m asl the bulk of gold assays are <2 ppm (in fact, below the 400 m asl level only three assays >2 ppm were recorded; Fig. 9). These low gold grades correlate with the narrow range in T_h seen in Fig. 8. Above 400 m asl the number of gold assays greater than 2 ppm increases and locally gold grades reach 57.9 ppm (Fig. 9). This zone correlates with the wide range in homogenisation temperatures (Fig. 8).

Another point to note, in addition to the two depth distributions of T_h data, is that the lowest homogenisation temperatures, at each sample depth, closely follow the +200-m-depth boiling curve.

Discussion

Mineralising processes

To assess the presence or absence of boiling phenomena in epithermal systems, Bodnar et al. (1985) state that the best evidence is the co-genetic existence of liquid- and vapour-rich fluid inclusions. However, the lack of vapour-rich inclusions should not be taken as evidence against boiling (e.g. Roedder 1984; Hedenquist and Henley 1985; Hedenquist et al. 1992). Also, the two inclusion types should show characteristic distributions of homogenisation temperatures. Liquid-rich inclusions exhibit bubble point homogenisation with a narrow temperature range. However, some exhibit anomalously high temperatures because of small amounts of vapour trapped along with the liquid. Conversely, the vapour-rich inclusions exhibit dew point homogenisation temperatures that show a scattered distribution, which is the result of vapour-rich inclusions trapping a variable amount of co-existing liquid. In addition, trends in homogenisation temperature and ice melting (salinity) are good indicators of boiling and/or mixing (e.g. Hedenquist and Henley 1985; Hedenquist et al. 1992; Simmons and Christenson 1994; Simeone and Simmons 1999).

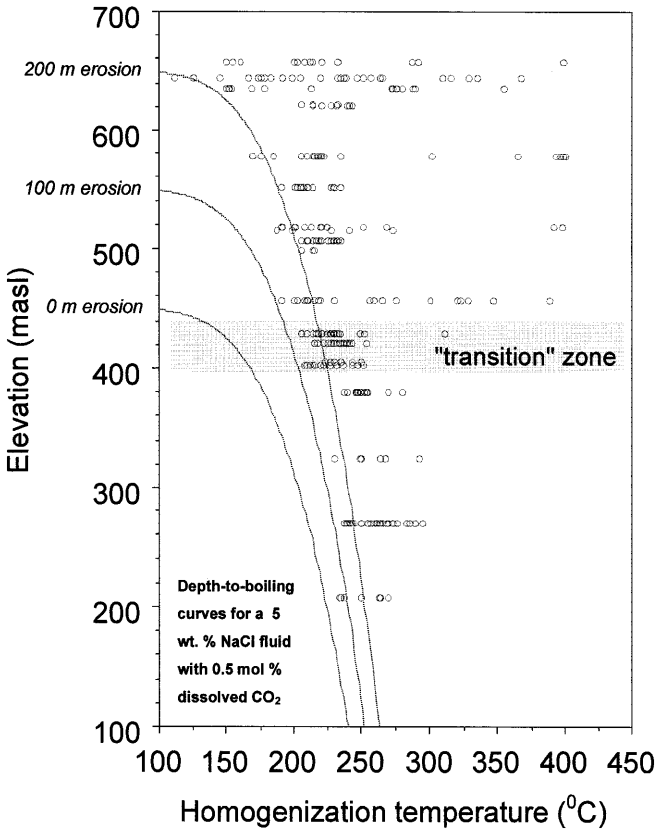

Fig. 8 Elevation–T_h relationships for ore-stage quartz fluid. Note that below 430 m asl elevation T_h data are tightly clustered and vary only by 25 to 50 °C, whereas above this level there is a much greater spread (up to 350 °C). Superimposed on the diagram are three boiling curves calculated assuming net erosion since mineralisation of 0, 100 and 200 m

Fluid inclusion evidence is not the only indication for boiling. Other criteria are used, and often needed for independent confirmation. Examples are the presence of platy calcite, quartz pseudomorphs after platy calcite (Browne 1978; Simmons and Christenson 1994) and/or adularia (Browne and Ellis 1970).

By using the above, it is possible to assess the role of boiling in the Profitis Ilias mineralisation. In the first instance, co-existing vapour- and liquid-rich inclusions were observed in quartz, suggesting that boiling may have occurred. However, the low frequency of this association makes it impossible to compare liquid and vapour homogenisation temperatures. Nonetheless, examination of Fig. 5C suggests that there is a high temperature 'tail' to the bubble point homogenisation data, indicating that some of the liquid-rich inclusions may have trapped small amounts of co-existing vapour. Also, vein textures (Fig. 3C) suggest boiling played a role in mineralisation as does the presence of adularia (Fig. 3A). In isolation, these observations do not indicate boiling as a major process. However, when they are combined with spatial and geochemical information, the case for boiling is much stronger (see Figs. 7 and 8).

The high-salinity trend

The high-salinity trend can be explained by either (1) mixing with an exotic brine (e.g. Simmons et al. 1988; Conrad et al. 1992) or (2) extensive boiling and vapourisation of a low salinity fluid (e.g. Simmons and Brown 1997; Scott and Watanabe 1998). Possible sources for the exotic brines are a magmatic fluid or a fluid that has interacted with evaporites. As there are no known evaporites within the stratigraphic sequence, it is hard to argue for this hypothesis. Mixing with a magmatic fluid is also difficult to invoke, as the microthermometric data (e.g. see Fig. 7) show that it would have to be between hot buoyant low-salinity 'meteoric waters' and cooler, dense 'magmatic brines'. A more probable explanation is extensive boiling of a low salinity fluid. In addition, the extensive boiling would have to be 'open system' to produce the observed range of salinities ('closed system' adiabatic boiling can only increase salinity by ~30%; Hedenquist and Henley 1985).

The high-T_h trend

The high-T_h trend can be explained by two processes: (1) heterogeneous trapping of liquid and vapour (steam) and (2) mixing between a relatively cool saline fluid and hot dilute fluid. Lack of high temperature alteration minerals (e.g. diopside; Deer et al. 1986) in the host rocks largely precludes the high-temperature (> 300 °C), low-salinity inclusions recording actual temperatures of mineralisation. Thus, the high temperatures are best explained through a mechanism of heterogeneous trapping of brine and co-existing vapour.

Fluid inclusion depth relationships

The data distribution in Fig. 8 is best explained by homogeneous and heterogeneous trapping of a boiling hydrothermal fluid. Below 430 m asl the hydrothermal fluid is boiling and loosing steam, leaving the residual fluid enriched in salt(s) (Fig. 7A, B, D, E). Here, only brine is trapped, resulting in relatively constant homogenisation temperatures and variable salinity. Then at ~430 to 450 m asl there is a transition zone, and above this elevation the hydrothermal fluid is in a region dominated by steam and inclusions trap both brine and steam. This results in the wide variation in homogenisation temperatures > 450 m asl (Fig. 8) and the high-T_h trend seen in Fig. 7F, I.

Scott and Watanabe (1998) observed very similar features in the Hokko low-sulphidation prospect in Japan. Homogenisation temperatures were widely variable (total variation: 87–168 °C) in the upper levels of the system, whilst in the lower levels they were more tightly constrained (total variation 34–100 °C). They also observed two T_h-salinity trends in their data that are similar, respectively, to the Profitis Ilias high-salinity and high-T_h trends.

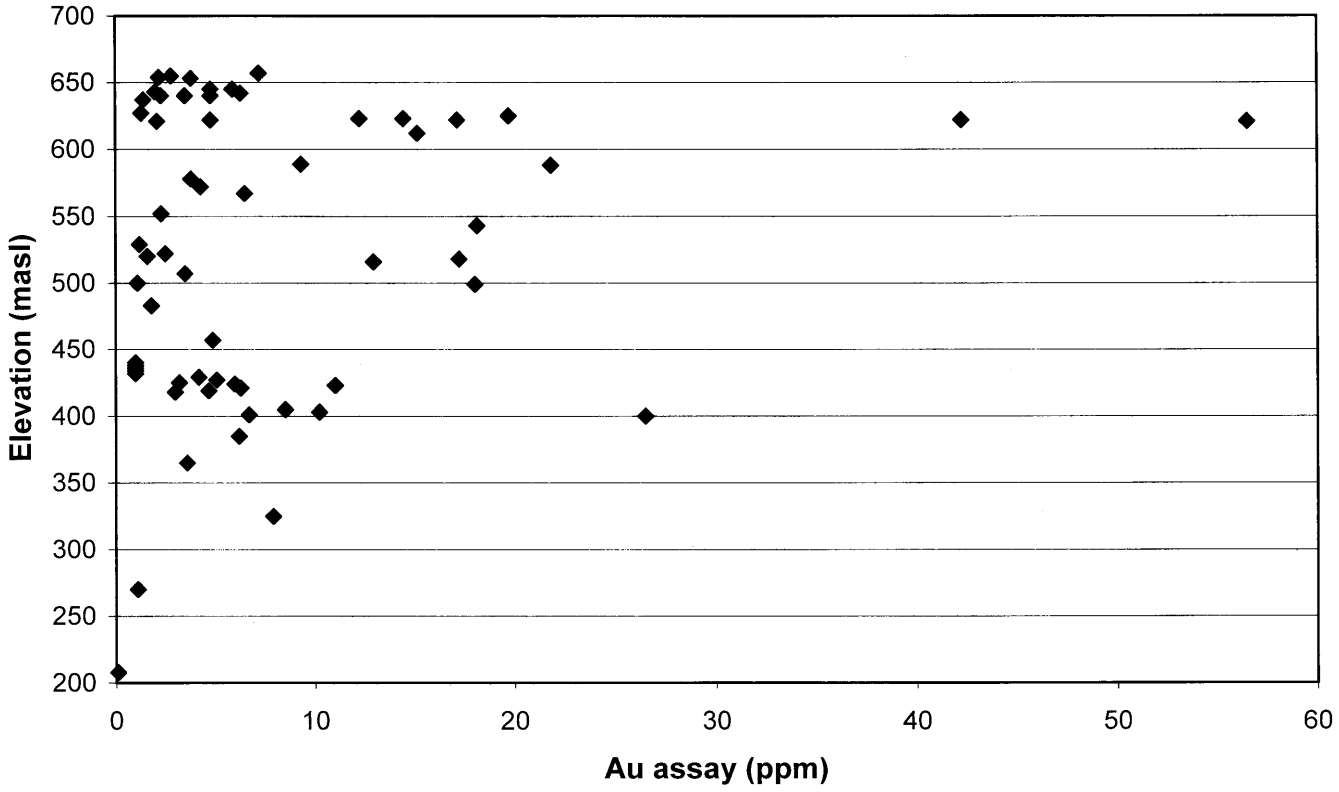

Fig. 9 Correlation between elevation and gold assay. Only assay values >2 ppm are plotted

Scott and Watanabe (1998) attributed these distributions to a process of extensive non-adiabatic boiling, vapourisation and steam loss in an open system. A similar explanation is probable for the microthermometric data from Profitis Ilias. Furthermore, Simmons and Browne (1997), in a fluid inclusion study of sphalerite from the Broadlands–Ohaaki geothermal field recorded steep sub-vertical trends in salinity-T_h data. These trends were also attributed to the almost complete vapourisation of dilute thermal water.

Thus, at Profitis Ilias, boiling is the most likely explanation of the microthermometric data. Furthermore, this is seen by assessing microthermometric-elevation data rather than through direct fluid inclusion petrography, microthermometric data and mineralogy. This may be termed cryptic boiling.

Comparison with the active geothermal system on Milos

Chemical and geophysical studies of the active geothermal system (e.g. Fytikas 1977; Liakopoulos 1987; Fytikas 1989; Fytikas et al. 1989; Liakopoulos et al. 1991; Pflumio et al. 1991; Christanis and St. Seymour 1995) show that:

1. The reservoir liquid, before phase separation is moderately saline (~9 wt% dissolved salts) and after phase separation the condensed vapour has a salinity of 0.12 wt% NaCl.
2. The residual liquid phase is dominated by sodium chloride (up to 14.3 wt% NaCl) with significant potassium (1.1 wt%) and calcium (0.5 wt%). Magnesium (1.36×10^{-4} mol/l) and sulphate (1.04×10^{-5} mol/l) are strongly depleted compared with seawater.
3. The hydrothermal fluid separates into liquid and vapour phases ('boils') during its ascent to the surface.
4. Stable ($\delta^{18}O$, δD), radiogenic ($^{87}Sr/^{86}Sr$) isotopes and hydro-geochemistry show that the dominant source for the modern geothermal fluid is seawater with minor meteoric and juvenile components.

Additionally, Christanis and St. Seymour (1995) have shown that the geothermal fluids are metalliferous. They identified Pb, Zn and Cu sulphides in scales from the experimental power plant and detected Ag by XRF analysis. Also, the geothermal fluids contain up to 1.5 ppb gold (Liakopoulos 1987).

The paleo-geothermal system preserved at Profitis Ilias exhibits a number of characteristics in common with the modern system:

1. Estimated salinities (0.0–11.3 wt% NaCl equiv.) are similar. Also, the lowest salinities are associated with inclusions from the 'heterogeneous trapping' zone. This is equivalent to the condensed vapour in the modern system.
2. Ice and first melting observations in fluid inclusions show that the paleo-fluid is dominated by sodium chloride with some di-valent cations (Ca or Mg) (see Fig. 5A). Analyses of the modern geothermal fluid show that it is also dominated by sodium chloride with significant calcium.

3. There is good evidence that the paleo-geothermal fluids boiled (see Fig. 7). In the modern system, the geothermal fluids boil on their ascent to the surface.

Thus the paleo-system at Profitis Ilias, as evidenced by fluid inclusion data, is broadly similar in terms of physico-chemical properties, to the modern geothermal system. Further evidence is provided by the analysis of the reservoir fluid (Liakopoulos 1987) and scales in the geothermal plant (Christanis and St. Seymour 1995). These show that the modern system is capable of transporting and depositing metals. In addition, the temperature of scale formation (200–230 °C) is very close to the estimated temperature for the mineralisation at Profitis Ilias (200–250 °C). This suggests that during boiling, the Profitis Ilias fluid would also be capable of depositing significant amounts of metal.

Comparisons between the modern geothermal system and mineralisation at Cape Vani (Mn–Ba) and Triades-Galana (Ag–Pb–Zn–Ba) have been made by Liakopoulos (1987), Liakopoulos and Boulegue (1987), Pflumio et al. (1991) and Christanis and St. Seymour (1995). They observed a similarity between mineral parageneses in the ancient and modern systems and concluded that the mineral deposits were produced from hydrothermal fluids with comparable characteristics to the modern system.

The fluid inclusion data and the mineralogical results for Profitis Ilias further constrain this hypothesis. They show that the modern and ancient systems are not only comparable in terms of their mineralogy and paragenesis but, moreover, they are analogous in terms of their physico-chemical properties. This parallelism between the ancient and modern systems suggests that since the earliest (Late Pliocene, ~3 Ma) volcanism on Milos, the region has been geothermally active. It is also probable that the processes of metalliferous mineralisation are likewise continuous. In addition, as seawater has been identified as a major fluid source in the modern system, then the above similarities also suggest that this may be the case for the Profitis Ilias hydrothermal fluids. Furthermore, at Profitis Ilias the lowest salinities in the high-salinity boiling trend are close to that of seawater, suggesting that this could have been the reservoir fluid at Profitis Ilias. Although, without corroborating isotopic data, this hypothesis cannot be confirmed.

Conclusions

The Profitis Ilias gold deposit occurs in a series of steep interconnected quartz veins formed within an epithermal environment. Estimated reserves amount to 5 million tonnes, grading 4.4 g/tonnes gold and 43 ppm silver.

Three broad stages of the mineralisation are recognised:

1. pre-ore stage: barren microcrystalline quartz + pyrite;
2. ore-stage: fine-grained and vuggy quartz + base metal sulphides ± native gold;
3. post-ore stage: fine-grained quartz + barite ± sulphides.

Electrum and sulphides tend to occur within finer-grained quartz rather than in the coarser vuggy quartz.

Based on the depth-T_h–salinity relationships, it is concluded that the hydrothermal fluids boiled between 200 and 250 °C and the salinity of the reservoir fluids was ~5 wt% NaCl equiv. (minimum salinity of the high salinity trend). There is also a zone, located at ~430–450 m asl, that marks the transition between the liquid- and vapour-dominated systems. Depth-to-boiling curves suggest that the elevation of the paleo-surface was ~200 m above the present summit of Profitis Ilias.

Extreme boiling and vapourisation probably played an important role in mineralisation and they provide the best explanation for the wide range in fluid inclusion salinities. Our data help confirm the importance of open system boiling in mineralised epithermal systems as suggested by Scott and Watanabe (1998).

The close association between gold and cryptic boiling in the hydrothermal fluids is only seen by examining the relationship between depth and homogenisation temperature data. Thus, in epithermal environments, this shows the importance of being able to correlate fluid inclusion data with depth and assay information.

Comparison of the mineralisation at Profitis Ilias with the modern geothermal system indicates that the processes of metal (Pb, Zn, Cu, Ag and Au) mineralisation are still occurring today and have probably been continuous since the Late Pliocence. However, the centres of geothermal activity have moved in space and time. Also, there are indications that the source of the mineralising fluid was seawater.

Acknowledgements Financial support by The British Council and the Greek General Secretariat of Research and Technology, through the 'Joint Research and Technology Programmes 1996–1997' Protocol between Britain and Greece, is gratefully acknowledged. S.F. Simmons and an anonymous reviewer are thanked for two constructive reviews that pointed us in the right direction and greatly improved the final version of the manuscript. Permission to publish for JN and TJS is granted by the Director, British Geological Survey, NERC.

References

Alfieris D (1993) The geology of Kalamavros–Koumaria–Chondro Vouno–Ag. Panteleimonas–Profitis Ilias–Mavrovouni area. Unpublished report, Silver and Baryte Ores Mining Co, Athens, Greece

Bodnar RJ (1993) Revised equation and table for determining the freezing-point depression of H_2O–NaCl solutions. Geochim Cosmochim Acta 57: 683–684

Bodnar RJ, Reynolds TJ, Kuehn CA (1985) Fluid inclusion systematics in epithermal systems. In: Berger BR, Bethke PM (eds) Geology and geochemistry of epithermal systems. Rev Econ Geol 2: 73–97

Briqueu L, Javoy M, Lancelot JR, Tatsumoto M (1986) Isotope geochemistry of recent magmatism in the Aegean arc: Sr, Nd, Hf, and O isotopic ratios in the lavas of Milos and Santorini – geodynamic implications. Earth Planet Sci Lett 80: 41–54

Browne PRL (1978) Hydrothermal alteration in geothermal fields. Annu Rev Earth Planet Sci 6: 229–250

Browne PRL, Ellis AJ (1970) The Ohaki–Broadlands hydrothermal area, New Zealand: mineralogy and related geochemistry. Am J Sci 269: 97–131

Christanis K, St. Seymour K (1995) A study of scale deposition: an analogue of meso- to epithermal ore formation in the volcano of Milos, Aegean Arc, Greece. Geothermics 24: 541–552

Christidis GE, Scott PW (1997) The origin and control of colour of white bentonites from the Aegean islands of Milos and Kimolos, Greece. Miner Deposita 32: 271–279

Christidis GE, Scott PW, Markopoulos T (1995) Origin of the bentonite deposits of eastern Milos, Aegean, Greece – geological, mineralogical and geochemical evidence. Clays Clay Miner 43: 63–77

Conrad ME, Petersen U, O'Neil JR (1992) Evolution of an Au–Ag-producing hydrothermal system: the Tayoltita mine, Durango, Mexico. Econ Geol 87: 1451–1474

Constantinidou H, Kilias S, Cheliotis I, Naden J, Shepherd T, Simos I, Crossing J (1998) Mineralogy and chemistry of gold in the Profitis Ilias epithermal deposit, Milos Island, Aegean Sea, Greece. Bull Geol Soc Greece XXXII(3): 157–164

Deer WA, Howie RA, Zussman J (1986) Rock forming minerals, vol 1B. Disilicates and ring silicates. Longman Group, London

Dewey JF, Sengor AMC (1979) Aegean and surrounding regions: complex multiplate and continuum tectonics in convergent zone. Geol Soc Am Bull 90: 84–92

Ellis AJ, Golding RM (1963) The solubility of carbon dioxide above 100 °C in water and in sodium chloride solutions. Am J Sci: 261: 481–489

Ericsson T, Papatheodorou K, Sklavounos S, Filippidis A (1992) Oxidation-state of biotite from heated perlite samples from Chivadolomni deposits in Milos island, Greece. Neues Jahrb Mineral Monatsh 1: 1–12

Fytikas M (1977) Geological and geothermal study of Milos island (in Greek with English abstract). Unpublished report, IGME Athens, Greece, XVII No 1

Fytikas M (1989) Updating of the geological and geothermal research on Milos island. Geothermics 18: 485–496

Fytikas M, Giuliani O, Innocenti F, Marinelli G, Mazzuoli R (1976) Geochronological data on recent magmatism of the Aegean Sea. Tectonophysics 31: 29–34

Fytikas M, Innocenti F, Manetti P, Mazzuoli R, Peccerillo A, Villari L (1984) Tertiary to Quaternary evolution of volcanism in the Aegean region. In: Dixon JE, Robertson AHF (eds) The geological evolution of the eastern Mediterranean. Geol Soc Lond Spec Publ 17: 687–699

Fytikas M, Innocenti F, Kolios N, Manetti P, Mazzuoli R, Poli G, Rita F, Villari L (1986) Volcanology and petrology of volcanic products from the island of Milos and neighbouring islets. J Volcanol Geotherm Res 28: 297–317

Fytikas M, Garnish JD, Hutton VRS, Staroste E, Wohlenberg J (1989) An integrated model for the geothermal field of Milos from geophysical experiments. Geothermics 18: 611–628

Galanopoulos V, Koinakis I (1991) Hydrothermal ores Mn + Ba + Fe of the Vani mine, Milos. Unpublished report, IGME Athens, Greece

Hauck M (1983) The barite deposits in the island of Milos (Aegean Sea), Greece. Fortschr Mineral 61: 81–82

Hedenquist JW, Henley RW (1985) The importance of CO_2 on freezing-point measurements of fluid inclusions – evidence from active geothermal systems and implications for epithermal ore deposition. Econ Geol 80: 1379–1406

Hedenquist JW, Reyes AG, Simmons SF, Taguchi S (1992) The thermal and geochemical structure of geothermal and epithermal systems: a framework for interpreting fluid inclusion data. Eur J Mineral 4: 989–1016

Jackson J, McKenzie D (1988) The relationship between plate motions and seismic moment tensors, and the rates of active deformation in the Mediterranean and Middle-East. Geophys J 93: 45–73

Le Pichon X, Angelier J (1979) The Hellenic arc and trench system: a key to the evolution of the eastern Mediterranean area. Tectonophysics 60: 1–42

Liakopoulos A (1987) Hydrothermalisme et mineralisations metalliferes de l'ile de Milos (Cyclades–Grece). PhD Thesis Univ Paris VI, pp 276

Liakopoulos A, Boulegue J (1987) A geochemical model for the origin of geothermal fluids and the genesis of mineral deposits on Milos Island. Terra Cognita 7: 228

Liakopoulos A, Katerinopoulos A, Markopoulos T, Boulegue J (1991) A mineralogical, petrographic and geochemical study of samples from wells in the geothermal field of Milos Island (Greece). Geothermics 20: 237–256

Liatsikas N (1955) Geology of some useful minerals of Milos Island. Inst Geol Min Res (IGMR), Athens, Greece. Geol Exped 20: 1–30

McKenzie D (1970) The plate tectonics of the Mediterranean region. Nature 226: 239–243

Morrisson GW, Rose WJ, Jaireth S (1991) Geological and geochemical controls on the silver content (fineness) of gold in gold–silver deposits. Ore Geol Rev 6: 333–364

Murray A, Petrakis A (1993) Sampling results of semi-regional exploration, southwest Milos. Unpublished report, Silver and Baryte Ores Mining Co, Athens, Greece

Papanikolaou D, Lekkas E, Syskakis D (1990) Tectonic analysis of the geothermal field of Milos island (in Greek). Bull Geol Soc Greece XXIV: 27–46

Papazachos CB, Comninakis PE (1971) Geophysical and tectonic features of the Aegean arc. J Geophys Res 76: 8517–8533

Papazachos CB, Kiratzi AA (1996) A detailed study of the active crustal deformation in the Aegean and surrounding area. Tectonophysics 253: 129–153

Pflumio C, Boulegue J, Liakopoulos A, Briqueu L (1991) Oxygen, hydrogen, strontium isotopes and metals in the present-day and past geothermal systems of Milos island (Aegean arc). In: Pagel M, Leroy JL (eds) Source, transport and deposition of metals. Balkema, Rotterdam, pp 107–112

Ramdohr P (1980) The ore minerals and their intergrowths, 2nd edn. International Series in Earth Sciences 35, Pergamon Press, Oxford

Roedder E (1984) Fluid inclusions. Rev Mineral, vol 12, Min Soc Am, Washington, DC

Scott A-M, Watanabe Y (1998) 'Extreme boiling' model for variable salinity of the Hokko low-sulphidation epithermal gold prospect, south-western Hokkaido, Japan. Miner Deposita 33: 568–578

Shepherd TJ, Bottrell SH, Miller MF (1991) Fluid inclusion volatiles as an exploration guide to black shale-hosted gold deposits, Dolgellau gold belt, North Wales, UK. J Geochem Explor 42: 5–24

Simeone R, Simmons SF (1999) Mineralogical and fluid inclusion studies of low-sulphidation veins at Osilo (Sardinia). Miner Deposita 34: 705–717

Simmons SF, Browne PRL (1997) Saline fluid inclusions in sphalerite from the Broadlands–Ohaaki geothermal system: a coincidental trapping of fluids evaporated to dryness. Econ Geol 92: 485–489

Simmons SF, Christenson BW (1994) Origins of calcite in a boiling geothermal system. Am J Sci 294: 361–400

Simmons SF, Gemmel JB, Sawkins FJ (1988) The Santo Nino silver–lead–zinc veins, Fresnillo district, Zacatecas, Mexico. Part 2. Physical and chemical nature of ore-forming fluids. Econ Geol 83: 1619–1641

Spartali E (1994) Current exploration for epithermal gold mineralisation in post-Tertiary volcanic rocks, Milos island, Greece. MSc Thesis, University of London

Sterner SM, Hall DL, Bodnar RJ (1988) Synthetic fluid inclusions .4. Solubility relations in the system NaCl–KCl–H_2O under vapor-saturated conditions. Geochim Cosmochim Acta 52: 989–1005

Tsokas GN (1996) Interpretation of the Bouguer anomaly of Milos island (Greece). J Volcanol Geotherm Res 72: 163–181

Voreadis G, Mourabas T (1935) The silver-bearing ores of Milos (in Greek). Unpublished report of Geol Surv Greece, no 22